Weld World (2015) 59:513–519
DOI 10.1007/s40194-015-0226-3

RESEARCH PAPER

Influence of boron and nitrogen on microstructure and hardness of heat-affected zone of modified 9Cr–1Mo steel—Gleeble simulation study

C. R. Das · A. K. Bhaduri · S. Lakshmi · S. Chakravarty · S. K. Kar · S. K. Albert

Received: 7 September 2014 / Accepted: 24 January 2015 / Published online: 11 February 2015

Abstract Microstructural evolution in three different boron-added modified 9Cr-1Mo (P91) steels has been studied after subjecting them to in different peak simulation conditions. Optical microscopy, scanning electron microscopy, and X-ray diffraction tools have been used to characterize the microstructure. Prior austenite grain boundaries are found to be present after heat treatments at 950–1200 °C, suggesting thereby that these boundaries are stable and that the "memory effect" exists in these steels. Analysis based on the modified Williamson–Hall plot shows that while the crystallite size remains similar irrespective of the peak simulation temperature, the highest peak simulation temperature results in lower dislocation density. The measured hardness values remain similar irrespective of the peak simulation temperature, except for marginal variations among the three different heats.

Keywords Steels · Boron · Austenite · Grain size · Dislocations · Density · Crystal structure · Simulating · X-rays · Diffraction

Doc. IIW-2538, recommended for publication by Commission II "Arc Welding and Filler Metals"

C. R. Das · A. K. Bhaduri (✉) · S. K. Albert
Materials Development and Technology Group, Indira Gandhi Centre for Atomic Research, Kalpakkam 603102, India
e-mail: arunkbhaduri@gmail.com

S. Lakshmi
PSG College of Technology, Coimbatore, India

S. Chakravarty
UGC-DAE CSR, Kokilamedu, Tamil Nadu, India

S. K. Kar
Indian Institute of Technology, Kharagpur, India

1 Introduction

Boron addition in ferritic steels to mitigate Type IV cracking is well reported [1–4]. Type IV cracking is the failure of weldment during creep/service exposure in the fine grain heat affected zone (FGHAZ) and/or inter critical HAZ (ICHAZ), due to lower creep strength of these regions compared to the coarse grain HAZ (CGHAZ) and base metal [5–8]. Attempts have been made to understand the microstructure of these HAZ regions and their effect on the creep properties by furnace heat treatment or Gleeble based simulation [9]. Although, in actual weldments, the dimensions of these HAZ regions are very small compared to that of the weld metal and the base metal, their role in determining the life of weldments at elevated temperatures is well established [10, 11]. While it is essential to characterize the microstructure and mechanical properties of individual HAZ regions to understand the deformation behavior of weldments, their small dimensions inhibit fabrication of specimens for mechanical testing. While physical simulation of the HAZ regions in a furnace at pre-set temperatures can produce more uniform microstructure over large dimensions compared to that in a Gleeble simulator [12], the heating rates achievable in a furnace are significantly less than in a Gleeble simulator in which heating rates achieved are similar to those experienced during actual welding. There exists a large hardness strength gradient across weld joints [1–3, 9–11], and as each HAZ (microstructural) region is surrounded by regions having different mechanical properties, deformation of lower strength regions (ICHAZ/FGHAZ) is restricted by high-strength regions around them [13]. This constraint leads to stress redistribution and development of multiaxial state of stress in the weldment thereby limiting its life [6, 13]. Therefore, fabricating weld joints with uniform microstructures having comparable mechanical properties across the HAZ would reduce the strength gradient and result in relatively uniform deformation and consequent increase in creep rupture life [4].

Table 1 Chemical composition (in wt%) of the boron-added P91 steels

	C	Cr	Mo	Si	Mn	Ni	V	Nb
P91B1	0.10	8.50	1.04	0.40	0.30	0.02	0.23	0.09
P91B2	0.092	9.00	1.00	0.35	0.40	0.01	0.20	0.07
P91B3	0.10	9.20	1.00	0.48	0.50	0.01	0.21	0.07
	N	B	P	S	Al	Cu	Fe	
P91B1	0.0021	0.010	0.005	0.002	0.03	0.006	Balance	
P91B2	0.0047	0.010	0.04	0.005	0.001	0.01	Balance	
P91B3	0.011	0.006	0.04	0.04	0.003	0.01	Balance	

Addition of boron to P91 steel produces a stable and relatively uniform microstructure across the HAZ [4]. To accrue the beneficial effects of boron, nitrogen content has to be reduced to ensure that the brittle boro-nitride phase does not form [4]. However, reduction in nitrogen content reduces volume fraction of MX-type precipitates that contributes to high-temperature creep strength. Therefore, nitrogen content has to be optimized to ensure increased volume fraction of MX-type precipitates without the formation of boro-nitrides. Also, boron significantly reduces the coarsening kinetics of $M_{23}C_6$ precipitates that contribute to reduction in the recovery of dislocations and consequent decrease in creep rate. Hence, both boron and nitrogen contents have to be optimized.

The objective of the work reported here is to understand the microstructural evolution in the temperature range 950–1,200 °C. The different microstructural regions of the HAZ were simulated in a Gleeble and characterized comprehensively using optical and scanning electron microscopy as also X-ray diffraction (XRD) studies.

2 Experimental

The 12-mm thick plates of three heats of boron-added P91 steel, with varying boron and nitrogen contents (Table 1), were produced by an Indian manufacturer. These plates, cut to 250×150×12 mm^3 size, were normalized at 1,100 °C for 1 h, tempered at 760 °C for 3 h, and then furnace cooled. Based on boron (60–100 ppm) and nitrogen (21–110 ppm) content, these base materials are designated as P91B1, P91B2, and P91B3 (Table 1). ThermoCalc was used to determine thermodynamic equilibrium transformation temperatures of these three steels using TCFe6 thermodynamic database. Dilatometry tests were carried out, with 4 mm diameter×10 mm long specimens, in argon atmosphere using a heating rate of 60 °C/s with no hold time at 1,050 °C. Gleeble simulations, using 10 mm diameter×100 mm long specimens, were carried out at peak temperatures of 950, 1,100, and 1,200 °C. The thermal cycle adopted involved heating to 200 °C at 20 °C/s and holding there for 10 s to simulate preheating, followed by heating to the peak temperature at 44 °C/s, and then cooling to 350 °C at 7.5 °C/s, then to 250 °C at 2.5 °C/s, followed by natural cooling. Diametrical changes were also monitored during the thermal cycle using a linear variable differential transducer attached to the specimen. All the simulated specimens were subjected to simulated post weld heat treatment at 760 °C for 3 h.

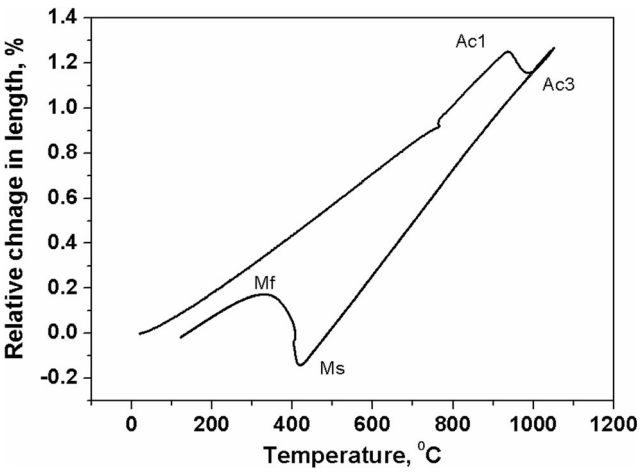

Fig. 1 Relative change in length during dilatometry test with temperature for P91B1 steel

XRD measurements were made on 10 mm diameter×5 mm long samples extracted from the centre of Gleeble simulated specimens that were polished up to 0.25 μm finish in diamond slurry. High-resolution XRD was carried out on a Bruker D8 Discover parallel-beam (operating at 45 kV×100 mA=4.5 kW) X-ray diffractometer using 6 kW rotating copper anode and step size of 0.04°. Microstructural examination was carried out using a CamScan 3200 scanning electron microscope. Hardness measurements were made with a Vicker's hardness tester at 200 g load, using polished specimens that were etched with Villella's reagent.

Table 2 Transformtion temperatures (in °C) for the boron-added P91 steels

	Ac_1	Ac_3	M_s	M_f
P91B1	909	979	412	275
P91B2	939	988	414	359
P91B3	931	979	399	360

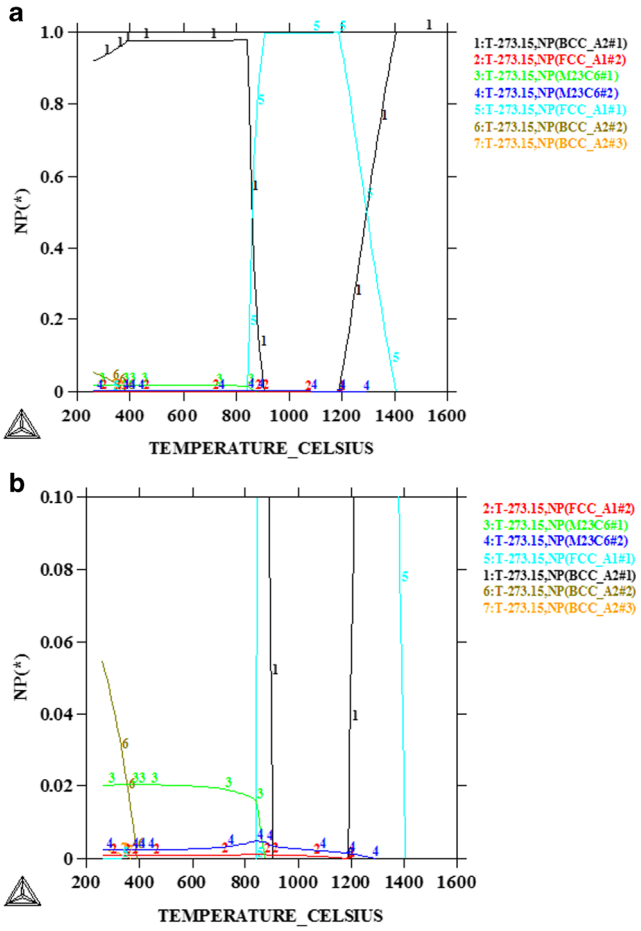

Fig. 2 Phase fraction in P91B1 steel calculated using ThermoCalc software with the *y* axis in: **a** linear scale from 0 to 1 and **b** linear scale from 0 to 0.1

3 Results and discussion

3.1 Dilatometry studies

The temperatures at which transformation to austenite starts and ends during heating, and to martensite starts and finishes during cooling, have practical implication while designing new alloy systems. The relative change in length as function of temperature $\Delta L/L_0 = f(T)$ is shown in Fig. 1 for P91B1 steel. Initially, the strain is zero, and with the increase in temperature, the strain increases and suddenly decreases at a point where $\alpha \rightarrow \gamma$ transformation begins. The temperature at which the slope deviates is denoted as A_{c1}. On subsequent heating to 1,050 °C, the slope again deviates at a point which is denoted as A_{c3} temperature. During cooling, contraction starts, and the temperature at which $\gamma \rightarrow \alpha'$ transformation starts, the slope deviates till completion of martensitic transformation, and these transformation temperatures are denoted as M_s and M_f. During martensitic transformation, the material expands, and hence, the slope changes. The transformation temperatures for the three steels (Table 2) show marginal variations attributable to the slight differences in their chemical composition.

3.2 ThermoCalc calculations

The phase stability diagram for P91B1 steel (Fig. 2) shows presence of $M_{23}C_6$, MX, and M_2B precipitates, with $M_{23}C_6$ and M_2B being found to be stable up to 900 and 1,100 °C, respectively, beyond which their stability decreases rapidly. This calculated diagram is found to be consistent with the phase state of the material, with the A_{c1} and A_{c3} equilibrium temperatures being estimated to be 839 and 896 °C, respectively. The amount of $M_{23}C_6$ at room temperature (RT) is ~1.7 wt% with

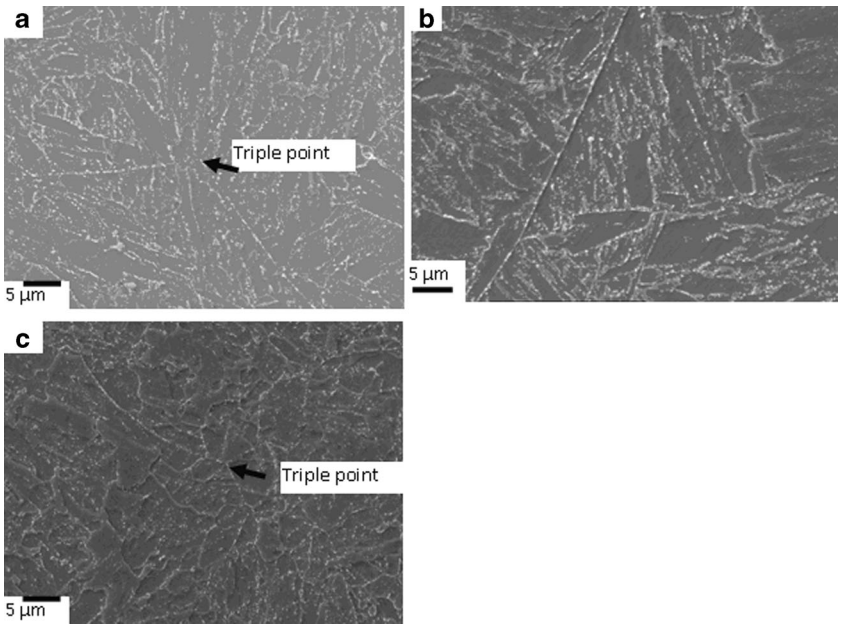

Fig. 3 Secondary electron images of **a** P91B1, **b** P91B2, and **c** P91B3 steels subjected to peak simulation temperature of 950 °C and tempering at 760 °C for 3 h

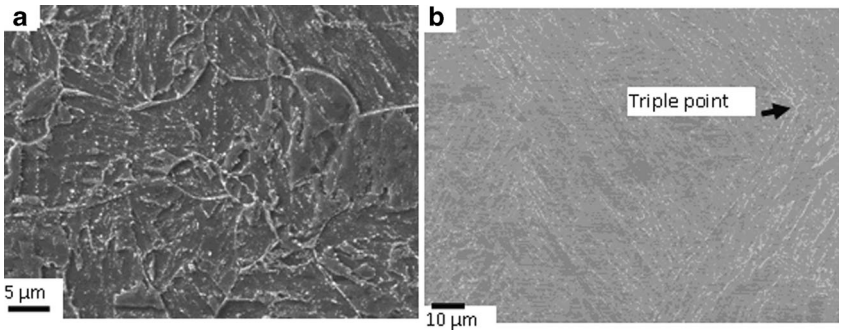

Fig. 4 Secondary electron images of **a** P91B2 and **b** P91B3 steels subjected to peak simulation temperature of 1,100 °C and tempering at 760 °C for 3 h

its solvus being at 878 °C, while that of M_2B at RT is ~0.18 wt% with its solvus being at 1,192 °C. ThermoCalc calculations predict that, after tempering at 760 °C, Laves phase, which is stable up to 620 °C, should be present. However, Lave phase is not observed in these steels.

ThermoCalc calculations also predict the presence of nitridic Z-phase, instead of MX carbonitrides, with the Z-phase being thermodynamically more stable than MX carbonitrides at about 800 °C. However, Z-phase starts to precipitate only after 10,000 h of exposure at 650 °C [14]. Loss of creep strength in P91 steel is commonly attributed to the precipitation of this Z-phase.

3.3 Microstructure

The microstructure of the normalized and tempered boron-added P91 steel consists of tempered lath martensite, with precipitates decorating the prior austenite grain (PAG) boundaries. The PAG boundaries and triple points are clearly discernible in the boron-added P91 steels after simulation at peak temperatures of 950 and 1,100 °C followed by 760 °C/3 h tempering (Figs. 3 and 4), suggesting that the original PAG boundaries are stable even after these simulation treatments. Simulation at a peak temperature of 1,200 °C and subsequent 760 °C/3 h tempering of P91B3 steel (Fig. 5) results in the formation of some new PAGs having size smaller than that in the base metal and after simulation at peak temperatures of 950 and 1,100 °C. While Fig. 5(a) shows the presence of coarse (>80 μm) as well as fine (~30 μm) PAGs, Fig. 5(b) shows the presence of the original PAG boundaries. Similar microstructural features are observed in the P91B1 and P91B2 steels are simulation at a peak temperature of 1,200 °C. It is evident from these observations that the boron-added P91 steels the PAG size remains intact to a great extent, albeit with some grain refinement, even after simulation at a peak temperature of 1,200 °C. In fact, grain refinement in boron-containing steel weldment is observed at the weld interface in the CGHAZ.

The formation of original PAGs of similar lath morphology after heat treatment at temperatures higher than the A_{c3} transformation temperature is referred to as the "memory effect" [15, 16], with addition of boron enhancing the "memory effect" in these steels [16].

3.4 XRD analyses

From XRD peak profiles for boron-added P91 steels simulated at peak temperatures of 950, 1,100, and 1,200 °C (Fig. 6a, b, c, respectively), it is evident that the intensity of NbC peak decreases at 1,200 °C suggesting that NbC precipitates dissolve during simulation at 1,200 °C. As MX-type precipitates are present in the normalized condition, these precipitates are stable at elevated temperatures [17]. The decrease in intensity of the (110) peak and increase in intensity of the (200) and (220) peaks, with increasing peak simulation temperature is also clear from these figures. The increase in intensity of (200) and (220) is attributed to texture effect [17].

XRD profiles provide information, such as peak position, peak broadening, and peak intensity. Any change in these parameters is related to changes in microstructure, which are expected to be present in the HAZ of weldments, as this regions experience varied peak temperatures causing microstructural changes during heating and cooling. The

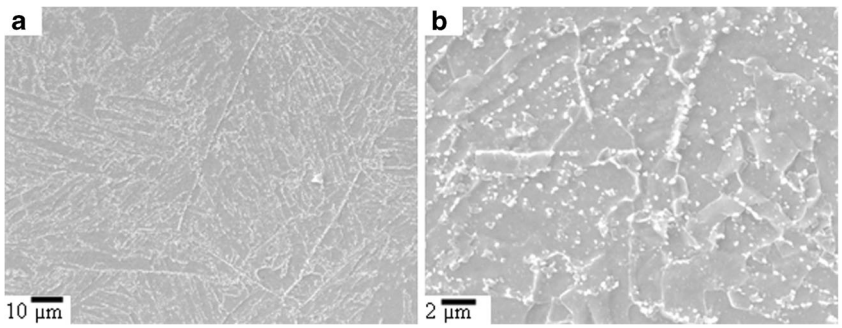

Fig. 5 Secondary electron image of P91B3 steel subjected to peak simulation temperature of 1,200 °C and tempering at 760 °C for 3 h

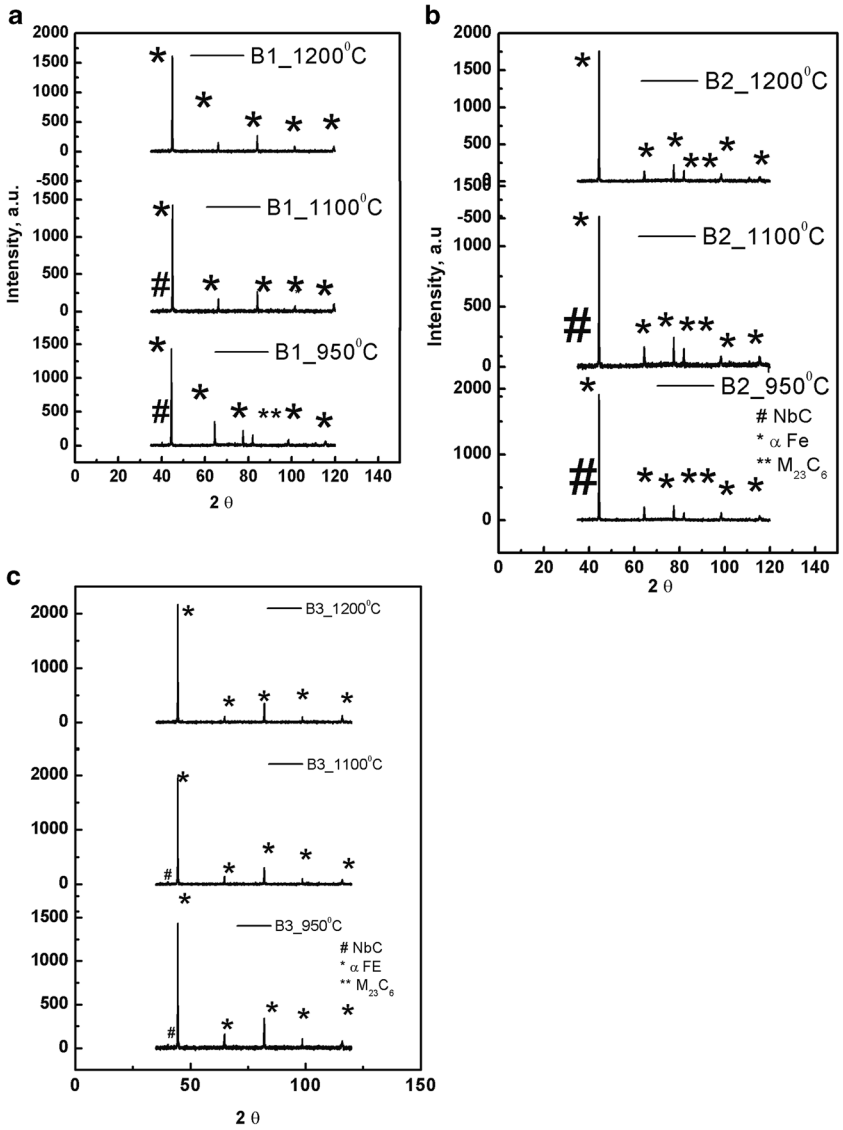

Fig. 6 XRD peak profiles of **a** P91B1, **b** P91B2, and **c** P91B3 steels subjected to different peak simulation temperatures

Williamson–Hall (W-H) plot shows the qualitative behavior of diffraction peak broadening using the full-width at half-maximum (FWHM) as a function of K, where $K=2\sin\theta/\lambda$, and θ and λ are the diffraction angle and wavelength of X-rays, respectively. The FWHMs are plotted as $\Delta K=2\cos\theta(-\Delta\theta)/\lambda$ (nm^{-1}) scale, where $\Delta\theta$ (in degrees) is the FWHM obtained from each (*hkl*) peak. The W-H peak broadening analysis suggests that the broadening of diffraction peak profile (ΔK, nm^{-1}) can be written as a combination of the grain size ($0.9/d$) and strain (ΔK^D) effects: $\Delta K=0.9/d+\Delta K^D$, where $K=1/d$, $\Delta K=-K(\Delta d/d)$, d (nm) is the average sub-grain (crystallite) and Δd (nm) is the FWHM obtained from the single peak fitting of the diffraction data. The W-H plot has been modified replacing K by K^2C based on the following equation [18, 19]:

$$(\Delta K)^2 = (0.9/d)^2 + (\pi A^2 b^2/2)\rho(K^2C) + O(K^2C)^2 \quad (1)$$

where A is a constant depending on the effective outer cutoff radius of dislocations, b is the Burgers vector of dislocation, ρ is the dislocation density, and O indicates non-interpreted higher order terms. Strain anisotropy among each (*hkl*) reflection has been rationalized by the

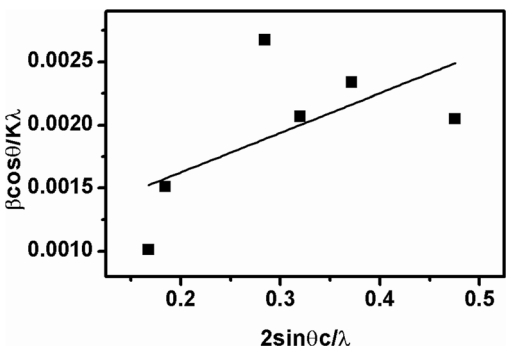

Fig. 7 Williamson and Hall plot for P91B1 steel

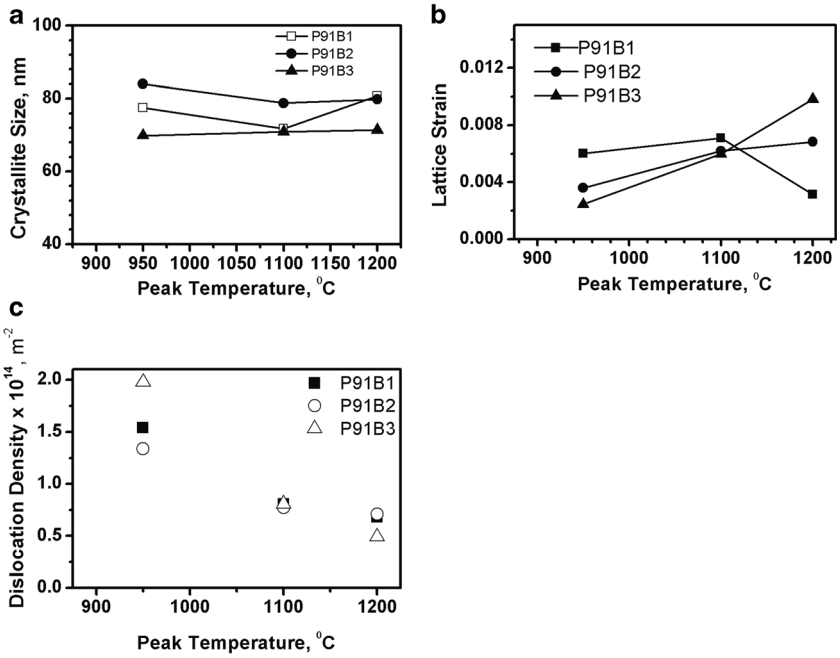

Fig. 8 Variation in **a** crystallite size, **b** lattice strain, and **c** dislocation density of boron-added P91 steels with peak simulation temperature

dislocation contrast factor (C) in modified W-H plot. The dislocation contrast factor (C_{hkl}) is reported to be a linear function of the (hkl) invariant of the reflections. It can be written as:

$$C_{hkl} = C_{h00}\left[1-q\left(h^2k^2 + h^2l^2 + k^2l^2/h^2 + k^2 + l^2\right)^2 \right. \quad (2)$$

C_{hkl} is presented as function of the q parameters in each (hkl) reflection. Putting C_{hkl} into Eq. 1 yields the theoretical calculation of ΔK. As a result, ΔK was modified and fitted among the (hkl) reflections as a function of K^2C.

The linear W-H plot assumes that both size and strain broadened profiles are Lorentzian in nature and provides information on the lattice strain (slope) and crystallite size (y-intercept=1/d), with Fig. 7 showing the modified W-H plot for P91B1 steel. With variation in peak simulation temperature, the crystallite/sub-grain size, estimated from peak profile analysis (Fig. 8a), remains similar with only a marginal reduction in size, with the sub-grain size for P91B3 steel being smaller than that for P91B1 and P91B2 steels. The sub-grain size of 100–200 nm is smaller than the lath size of 200–1,000 nm reported for 9%Cr steels [20]. The lattice strain is observed to increase with increase in peak simulation temperature (Fig. 8b), with the increase being more in P91B3 steel than in P91B1 and P91B2 steels. The lattice strain decreases at 1,200 °C for the P91B1 steel. The increase in lattice strain with peak simulation temperature can be attributed to the role of higher concentration of alloying elements increasing the lattice strain.

The dislocation density is observed to decrease with increase in peak simulation temperature (Fig. 8c). The dislocations that form during solid-state martensitic transformation are related to the transformation temperatures, with lower M_s and M_f temperatures resulting in higher dislocation density. The M_s and M_f temperatures obtained from C-strain dilatometry measurements (Table 3) show that these transformation temperatures decrease with increase in peak simulation temperature. These temperatures were obtained from cooling curve in C-strain measurement. Therefore, the material simulated at higher peak temperature would have higher dislocation density and easier annihilation of dislocations during the subsequent tempering. Hence, dislocation annihilation is less in the material simulated at a lower peak temperature, suggesting that dislocation density is

Table 3 Martensite start transformation temperatures for the boron-added P91 steels after simulation at different peak temperatures M_s

Peak simulation temperature (°C)	M_s temperature (°C)		
	P91B1	P91B2	P91B3
910	433	429	424
1100	381	384	390
1200	388	395	400

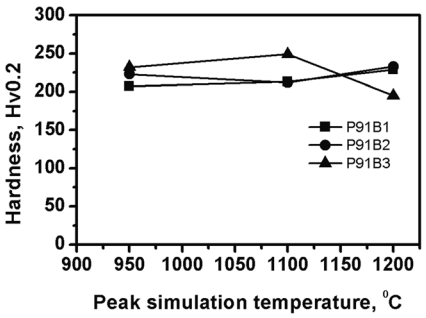

Fig. 9 Variation in hardness of boron-added P91 steels with peak simulation temperature

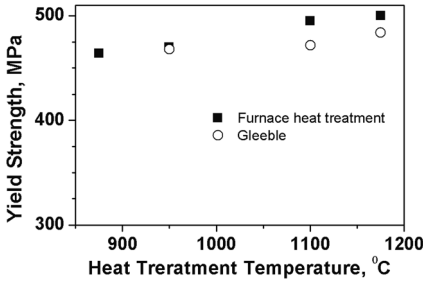

Fig. 10 Variation of yield strength with heat treatment/peak simulation temperature for P91B1 steel

higher in regions that experience lower temperatures such as in the ICHAZ. During simulation heat treatment, martensite transforms to austenite when A_{c3} temperature is crossed. As lower peak temperature leads to incomplete recrystallisation, the martensite that forms by retransformation of austenite during cooling has varied dislocation density. This could be one of the reasons for obtaining higher dislocation density in materials simulated at lower peak temperatures.

3.5 Structure property correlation

The hardness of the boron-added P91 steels is similar for materials simulated at different peak temperatures (Fig. 9), which is in agreement with their observed microstructural features. The variation in yield strength of P91B1 steel, obtained empirically from the hardness, with peak simulation temperature used for the Gleeble and furnace simulated specimens (Fig. 10) show that hardness/strength of the boron-added P91B steels remain similar except for a marginal increase with increase in peak simulation temperature.

The study shows that nitrogen and boron affect the crystallite size, lattice strain, and dislocation density in boron-added P91 steels. This variation in boron content in different heats causes variations in the recovery process, as increase in boron reduces the recovery of dislocations during tempering resulting in a finer crystallite size. This can explain the higher hardness observed in P91B3 steel compared to P91B1 and P91B2 steels (Fig. 9). Further, the similar strength levels of P91B1 steel in both Gleeble-simulated and furnace-simulated specimens suggest the stability of the boron-added P91 steels even when subjected to different heating rates.

4 Conclusions

(1) Uniform microstructures are observed in all these steels.
(2) Memory effect of the prior-austenite grains is observed in these steels.
(3) Prior-austenite size as a function of peak temperatures remains similar in all the three steels; with an increase in prior-austenite grain size, crystallite size was observed to have increased in peak simulation temperature for a given steel.
(4) The dislocation density decreases with increase in peak simulation temperature.
(5) Hardness/yield strength remains similar with marginal variation as a function of peak simulation temperature.
(6) Nitrogen and boron contents affect the crystallite size, lattice strain, and dislocation density in boron added P91 steel.

References

1. Abe F (2008) Sci Technol Adv Mater 9:013002, 15 pp
2. Abe F, Horiuchi T, Taneike M, Sawada K (2004) Mater Sci Eng A 378:299–303
3. Abe F, Tabuchi M, Kondo M, Tsukamoto S (2007) Int J Pressure Vessels and Piping 84:44–52
4. Das CR, Albert SK, Swaminathan J, Raju S, Bhaduri AK, Murty BS (2011) Metall Mater Trans A 42:3863–3866
5. Watanabe T, Tabuchi M, Yamazaki M (2006) Int J Pressure Vessels and Piping 83:63–71
6. Laha K, Chandravathi KS, Parameswaran P, Goyal S, Mathew MD (2012) Metall Mater Trans A 43:1174–1186
7. David SA, Siefert JA, Feng Z (2013) Sci Technol Welding and Joining 18:631–651
8. Parker J (2013) Mater Sci Eng A 578:430–437
9. Albert SK, Tabuchi M, Hongo H, Watanabe T, Kubo K, Matsui M (2003) Int J Pressure Vessels and Piping 20:405–413
10. Kojima T, Hayashi K, Kajita Y (1995) ISIJ Int 35:1284–1290
11. Laha K, Chandravathi KS, Parameswaran P, Rao KBS, Mannan SL (2007) Metall Mater Trans A 38:58–68
12. Das CR, Albert SK, Bhaduri AK, Murty BS (2013) Metall Mater Trans A 44:2179–2186
13. Divya M, Das CR, Albert SK, Goyal Sunil, Ganesh P, Kaul R, Swaminathan J, Murty BS, Kukreja LM, Bhaduri AK (2014) Mater Sci Eng A 613:148–158
14. Sawada K, Kushima H, Tabuchi M, Kimura K (2011) Mater Sci Eng A 528:5511–5518
15. T. Shirane, S. Tsukamoto, K. Tsuzaki, Y. Adachi, T. Hanamura, M. Shimizu and F. Abe, IIW Doc. IX-2246-07 (2007).
16. Kimmins ST, Gooch DJ (1983) Metal Sci 17:519–521
17. Yamada K, Igarashi M, Muneki S, Abe F (2002) ISIJ Int 42:779–784
18. Ungar T, Borbely A (1996) Appl Phys Lett 69:3173–3175
19. Woo W, Ungar T, Feng Z, Kenik E, Clausen B (2010) Metall Trans A 41:1210–1216
20. Tamura M, Haruguchi Y, Yamashita M, Nagaoka Y, Ohinata K, Ohnishi K, Itoh E, Ito H, Shinozuka K, Esaka H (2006) ISIJ Int 46: 1693–1702